Land-cover Classification of Suburban Areas Based on Multi-polarized Airborne SAR Data Using Texture Measures

Fumio Yamazaki, Natsuki Samuta, and Wen Liu
Department of Urban Environment Systems, Chiba University, Chiba, Japan

Abstract— Synthetic Aperture Radar (SAR) sensors onboard space-borne and airborne platforms are useful to survey the land-cover and condition of the earth surface. The Japan Aerospace Exploration Agency (JAXA) has been operating L-band radar systems both on satellites and aircrafts. The Polarimetric and Interferometric Airborne Synthetic Aperture Radar (Pi-SAR) L2 started its operation in 2012, as a successor of Pi-SAR-L (1996–2011). Pi-SAR-L2 carries an L-band radar of 85.0 MHz band-width and can acquire images of very high slant-range resolution 1.76 m with full (HH, HV, VV, VH) polarizations. In this study, a basic study on backscattering characteristics of a suburban area was carried out using full polarization data acquired by Pi-SAR-L2 flying over Miyagi prefecture, Japan. The texture measures of the SAR data were obtained by the Gray Level Co-occurrence Matrix (GLCM), which is one of the most well-known texture measures in the recent years. The selected major land-cover classes were trees, grasses, roads, water, paddy fields, buildings and solar panels. The result of supervised classification shows that the combined use of the backscattering intensity and their texture measures could obtain higher accuracy than using only the backscattering intensity.

1. INTRODUCTION

Remote sensing technologies have been used for various objectives, such as land-use and land-cover classifications, disaster risk assessment and emergency response, and traffic monitoring and city planning. There are mainly two categories of remote sensing from the sensor type: passive (optical and thermal sensors) and active (mainly radar sensors) remote sensing [1, 2]. Optical satellite systems work in the daytime and cannot observe objects under cloud-cover conditions. However, a radar system as Synthetic Aperture Radar (SAR) overcomes this problem and has been used in all day and all weather conditions [3, 4] Several frequency bands have been commonly used for satellite SAR systems, such as L-band (1–2 GHz: JERS-1, ALOS_PALSAR, ALOS-2_PALSAR-2), C-band (4–8 GHz: ERS-1/2, ENVISAT, Radarsat-1/2, RISAT-1, Sentinel-1), and X-band (8–12 GHz: TerraSAR-X, COSMO-SkyMed). Among these frequency bands, the L-band is suitable to observe coherent changes such as ground deformation while the X-band is suitable to observe manmade objects and small-scale changes [5].

In the recent years, airborne SAR systems have also been developed and used as an experimental phase. The Japan Aerospace Exploration Agency (JAXA) had operated Pi-SAR-L (Polarimetric and Interferometric Airborne Synthetic Aperture Radar) from 1996 to 2011 [6]. Pi-SAR-L2, the successor of Pi-SAR-L, has been in operation since 2012 and has already acquired many scenes of natural and built environments [7]. Among them, we used a full-polarimetric Pi-SAR-L2 intensity image, acquired over a suburban area of Sendai city, Miyagi prefecture, Japan in June 2014, since this area was hit by the 11 March 2011 Tohoku earthquake and tsunami [5] and various multi-temporal remote sensing data are available.

In this study, land-cover classification was carried out using the full-polarimetric (HH, HV, VV and VH) Pi-SAR-L2 data and their texture measures [8–10]. The textures depend on spatial relation, scale and orientation of objects, and hence they are important attributes for SAR image classification because various features such as built-up urban, water, soil, and vegetation can be characterized easily. The characteristics of the Pi-SAR-L2 data were investigated through the principal component analysis (PCA) and the significant components were extracted. Then the supervised land-cover classification was carried out and the result was compared with the truth data made from optical images.

2. THE STUDY AREA AND DATA USED

The study area of this research is a part of Natori and Iwanuma cities, including Sendai airport. Fig. 1 shows a color composite (Red: HH polarization, Green: HV pol., Blue: VV pol.) of the Pi-SAR-L2 images acquired by a flight conducted by JAXA in the noon time (12:38:35–12:46:54) on June 12, 2014. The PiSAR-L2 flight took an ascending path with the left look, as shown in the

figure. The airborne SAR imagery data were obtained by the L-band with the center frequency of 85 MHz and have the slant-range resolution of 1.76 m and the azimuth resolution of 3.2 m. The obtained digital number (DN) of each polarization was converted to the backscattering coefficient (sigma naught, σ^0) in the groundrange of 2.5-m pixel size, with the decibel (dB) unit, represented by the following equation.

$$\sigma^0 = 10.0 \log_{10}\langle DN^2 \rangle + CF \tag{1}$$

where CF is the calibration factor determined as -81 dB by JAXA [7, 11] After this conversion, an adaptive Lee filter [12] of 3×3 was applied to the original SAR images to reduce the speckle noise.

Figure 2 shows an optical image of the study area and ground photos in our field survey on the day of the airborne SAR flight. This area was hit by the 11 March 2011 Tohoku earthquake and repeated tsunamis [5], and the flooded sea water remained for several days to several months. But the area had been partially restored, especially for agricultural lands, at the time of the airborne flight. Rice paddy fields had already been watered and planted. But new development of buildings and urban land-use was still underway. A large scale construction works of landfill and memorial parks were carried out when we visited there.

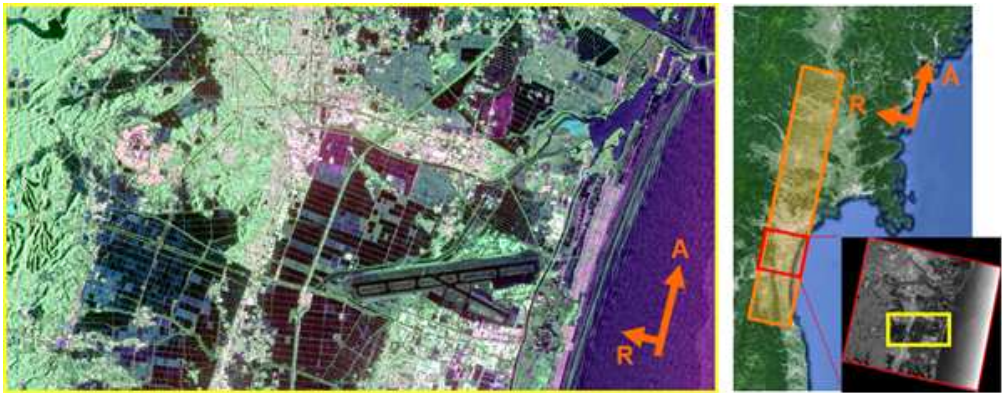

Figure 1. Color composite (R: HH, G: HV, B: VV) of multi-polarized Pi-SAR-L2 image taken on June 12, 2014 and the location of the study area in Natori and Iwanuma cities, Miyagi prefecture, Japan.

Figure 2. Optical image of the study area from Google Earth, acquired on Sept. 15, 2014, and ground photos taken in the field survey by the authors on June 12, 2014 ((a) residential area, (b) tsunami affected residential area, (c) Sendai Airport).

3. PRINCIPAL COMPONENT ANALYSIS FOR FULL-POLARIZATION IMAGES

The relationship among the four polarization data was first examined. The scatter plots between the HH and VV polarizations and HV and VH polarizations are shown in Figs. 3(a) and (b). As expected, the HH and VV polarizations exhibit similar backscattering values, and the HV and VH polarizations are even closer each other. The principal component analysis (PCA) was also

carried out for the full polarization image, and its result is shown in Fig. 3(c), where the cumulative Eigen values reached 91.9% for the first component, 97.5% until the second component, 99.9% until the third component, and of course 100% until the fourth component. Thus it is considered to be reasonable to select HH and HV polarizations out of the four polarizations for a further land-cover classification.

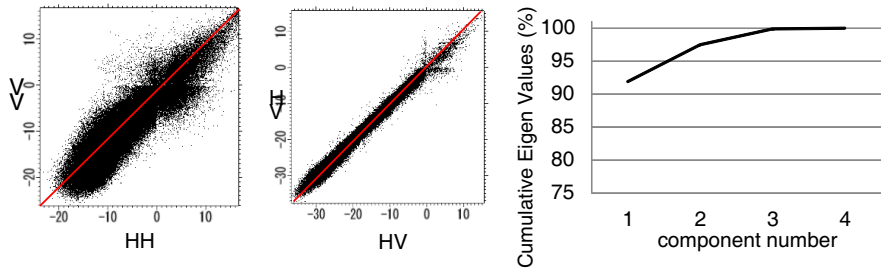

(a) HH vs VV (b) HV vs VH (c) Cumulative Eigen values

Figure 3. Scatter plots of HH and VV polarizations (a) and HV and VH polarizations (b) in dB unit, and cumulative Eigen values for the full-polarization images.

4. TEXTURE ANALYSIS FOR HH AND HV POLARIZATIONS

The texture measures are vital information from radar imagery [8–10]. Among several statistical texture methods proposed before, the gray-level co-occurrence matrix (GLCM) is one of the most powerful one for land-cover monitoring [8]. In this study eight textural features in angle 0°, distance 1, and a window size of 9×9 were calculated using ENVI software as follows:

$$Mean = \Sigma_{i=2}^{2N_g} i P_{x+y}(i) \tag{2}$$

$$Variance = \Sigma_i \Sigma_j (i-\mu)^2 P(i,j) \tag{3}$$

$$Homogeneity = \Sigma_i \Sigma_j \frac{1}{1+(i-j)^2} P(i,j) \tag{4}$$

$$Contrast = \Sigma_{N=0}^{N_{g-1}} n^2 \left\{ \Sigma_{i=1}^{N_g} \Sigma_{j=1}^{N_g} P(i,j) \right\} \quad |i-j| = n \tag{5}$$

$$Dissimilarity = \Sigma_{i,j=0}^{N_{g-1}} P_{i,j}(-\ln P_{i,j}) \tag{6}$$

$$Entropy = -\Sigma_i \Sigma_j P(i,j) \log(P(i,j)) \tag{7}$$

$$Angular\ Second\ Moment = \Sigma_i \Sigma_j \{P(i,j)\}^2 \tag{8}$$

$$Correlation = \frac{\Sigma_i \Sigma_j (i,j) P(i,j) - \mu_x \mu_y}{\sigma_x \sigma_y} \tag{9}$$

Figure 4 shows the eight texture measures calculated for the HH polarization sigma naught image. As expected, these texture measures have correlation with the original image and with the other texture measures. Hence the PCA was carried out again for the eight texture measures for the HH and HV polarizations, respectively. Fig. 5 shows the cumulative eigenvalues of the eight principal components for the HH polarization, in which the cumulative eigenvalues reached 75.0% for the first component, 93.1% until the second component, 99.9% until the third component. Considering the contribution ratio of each texture measure for the first three principal components, *Variance*, *Mean*, and *Contrast* were selected as the most significant texture measures for the HH polarization in this example, and their histograms are also shown in the figure.

The result of PCA for the HV polarization was similar as that for HH polarization. The cumulative Eigen values reached 67.4% for the first component, 93.5% until the second component, 99.9% until the third component. The contribution ratio of each texture measure for the first three principal components were also *Variance*, *Mean*, and *Contrast*.

5. LAND COVER CLASSIFICATION WITH AND WITHOUT TEXTURE MEASURES

Land cover classification was carried out for the study area to investigate the effects of use of the texture measures. First unsupervised classification by the K-means method was carried out the

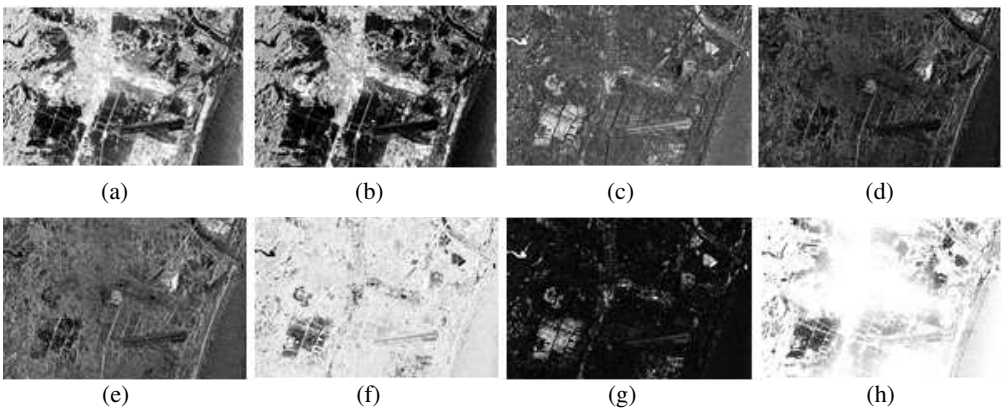

Figure 4. Eight texture measures calculated for the HH polarization Pi-SAR-L2 image for the study area. (a) Mean, (b) variance, (c) homogeneity, (d) contrast, (e) dissimilarity, (f) entropy, (g) angular second moment, (h) correlation.

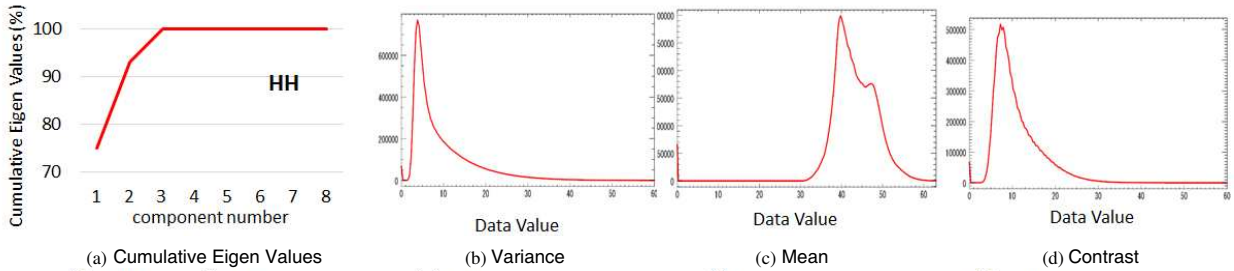

Figure 5. Cumulative Eigen values of the eight principal components for the eight textures of the HH polarization (a) and histograms of the three significant textures: Variance (b), Mean (c), and Contrast (d).

dual polarization (HH and HV) data. Several class numbers were tried and then the number of land cover classes was determined as seven as *tree*, *grass*, *road*, *water*, *rice paddy field*, *building* (*urban*), and *solar panel*

Object-based supervised classification was then carried out based on the Nearest Neighbor (KN) method, by employing training data shown in Fig. 6, where 20 to 30 objects were selected for each class other than solar panel. Since solar panels showed distinct backscattering characteristics, training data were selected from two locations of mega solar plants in the pink color circles. In object-based classification, the merge-level was set as 80 and the scale-level as 20.

The results of supervised classification are shown in Fig. 7 when using the HH and HV original images only, and in Fig. 8 when using the two original data plus 6 textures (*Variance*, *Mean*, and *Contrast* for HH and HV). These results look similar, especially for *buildings*, *trees*, and *rice paddy*. But some improvements by introducing the textures can be seen in *grass*, *water*, and a significant reduction of false positive error is observed for *solar panels*.

The PCA was further carried out for the set of 32 images with 4-polarizations times 8-texture

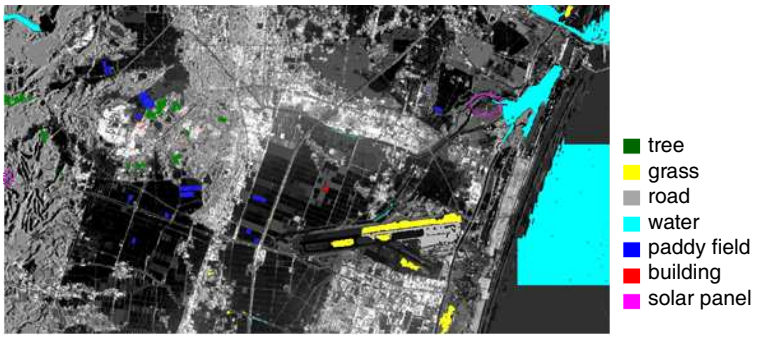

Figure 6. Training data for supervised classification of seven land-cover classes.

measures. The cumulative eigenvalues reached 95.5% for the first 5 principal components, and 99.9% for the first 8 components out of a total 32 components. Thus, the first 5 principal components out of 32 were employed together with the first 2 principal components of the original full-polarizations. The result of this classification is shown in Fig. 9. Some improvements are seen in this classification result because the effects of the VV polarization have been introduced.

Finally, this classification result was compared with the existing land-cover map produced by JAXA [13] using ALOS AVNIR-2 optical satellite images taken before the 2011 Tohoku earthquake [14]. In this land-cover map, only one urban land-cover class exists, and hence *road*, *building* and *solar panel* classes of Fig. 9 were merged as *urban* class.

Figure 10 compares the JAXA's land-cover map and our supervised classification result for five land cover classes (produced from Fig. 9), and the confusion matrix for the study area is shown in Table 1. From the table, the overall accuracy is about 50%, not so high, but higher than the case only HH and HV original data were used (43.0%). The producer accuracies of urban (74.2%), tree (65.9%), and water (79.8%) classes are high. It is noticed that grass class has low producer (4.7%) and user (4.4%) accuracies. The reason for this observation is rather complicated. The JAXA map was made before the 2011 tsunami inundation while our classification data were in the recovery stage. The JAXA map is not very accurate as its overall accuracy of 78.0% for 10-m grid

Figure 7. Supervised land-cover classification result for the original HH and HV polarization images.

Figure 8. Supervised land-cover classification result for the original HH and HV polarization images plus their texture measures (*Variance, Mean*, and *Contrast*).

Figure 9. Supervised land-cover classification result for the first two PC images of the original full-polarizations plus first five PC images of their texture measures.

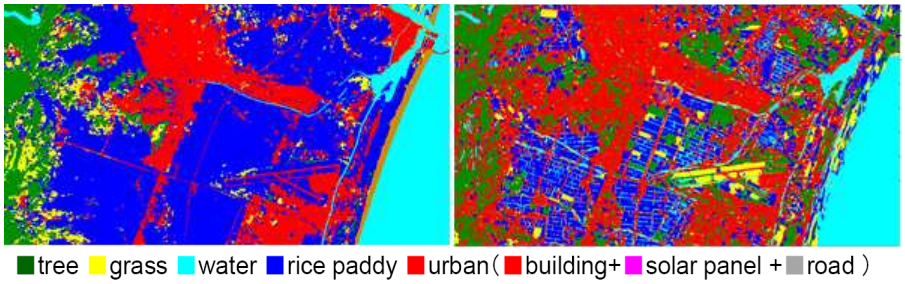

Figure 10. Comparison of JAXA's land-cover map of Japan [13] made from optical satellite images (left) and our classification result from Pi-SAR-L2 (right) for five land-cover classes.

cell [14]. Both grass and road classes show low SAR backscatter, but they have quite different spectral characteristics in optical images. The three land-cover classes merged as urban class have quite different SAR backscatter. These several reasons are considered as the cause of not so high accuracy. A selection of proper truth data suitable for land-cover classification results from SAR data should also be necessary.

Table 1. Confusion matrix between the land-cover map produced by JAXA [13] and our classification result from Pi-SAR-L2 for five land-cover classes.

Ground Truth (No. of pixels)							
class	urban	tree	rice paddy	grass	water	**total**	**Userb's Accuracy**
urban	**1854985**	266761	1845772	368944	66872	4403334	42.1%
tree	312170	**598704**	951649	165468	84648	2112639	28.3%
rice paddy	171457	14825	**1869822**	62274	77393	2195771	85.2%
grass	116061	15976	451047	**30104**	64814	678002	4.4%
water	51479	11962	460494	18966	**1155841**	1698742	68.0%
total	2506152	908228	5578784	645756	1449568	**11088488**	
Producerb's Accuracy	74.2 %	65.9 %	33.5 %	4.7 %	79.8 %	**Overall Accuracy 49.7%**	

6. CONCLUSION

In this study, land cover classification was conducted using full-polarization SAR data, obtained by JAXA's airborne radar system, Pi-SARL2. The SAR system carries L-band radar of 85.0 MHz band-width and can acquire images of very high slant-range resolution, 1.76 m In this study, a basic study on backscattering characteristics of a suburban area of Miyagi prefecture, Japan was carried out. First, the principal component analysis was applied to full-polarization imagery data and the first two components were found to be significant. Then the texture measures of the original SAR data were obtained by the Gray Level Co-occurrence Matrix (GLCM) and the principal component analysis was also applied to the eight texture measures. An object-based supervised land-cover classification was then applied to the principal components of the original full-polarization data and their texture measures. The result of the supervised classification was compared with the existing land-cover map, produced by JAXA from optical satellite images and the combined use of the original backscattering data and their texture measures could obtain higher accuracy than using only the original backscatter data.

ACKNOWLEDGMENT

The Pi-SAR-L2 data used in this study are owned by Japan Aerospace Exploration Agency (JAXA), and were provided through the JAXA's Pi-SAR-L2 research program (RA5, PI No. 2055). This

study was financially supported by the CREST program by the Japan Science and Technology Agency (JST) "Establishing the most advanced disaster reduction management system by fusion of real-time disaster simulation and big data assimilation (Research Director: Prof. S. Koshimura of Tohoku University)".

REFERENCES

1. Rathje, E. and B. J. Adams, "The role of remote sensing in earthquake science and engineering, opportunities and challenges," *Earthquake Spectra*, Vol. 24, No. 2, 471–492, 2008.
2. Dell'Acqua, F. and P. Gamba, "Remote sensing and earthquake damage assessment: Experiences, limits, and perspectives," *Proceedings of the IEEE*, Vol. 100, No. 10, 2876–2890, 2012.
3. Matsuoka, M. and F. Yamazaki, "Comparative analysis for detecting areas with building damage from several destructive earthquakes using satellite synthetic aperture radar images," *Journal of Applied Remote Sensing*, Vol. 4, 041867, SPIE, doi:10.1117/1.3525581, 2010.
4. Wieland, M., W. Liu, and F. Yamazaki, "Learning change from synthetic aperture radar images: Performance evaluation of a support vector machine to detect earthquake and tsunami-induced changes," *Remote Sensing*, Vol. 8, No. 10, 792, MPDI, doi:10.3390/rs8100792, 2016.
5. Liu, W., F. Yamazaki, H. Gokom, and S. Koshimura, "Extraction of tsunami-flooded areas and damaged buildings in the 2011 Tohoku-Oki earthquake from TerraSAR-X intensity images," *Earthquake Spectra*, Vol. 29, No. S1, S183–S200, 2013.
6. JAXA, "Pi-SAR", http://www.eorc.jaxa.jp/ALOS/Pi-SAR/about_pisar.html (accessed on 2017/2/5).
7. JAXA, "Pi-SAR-L2", http://www.eorc.jaxa.jp/ALOS/Pi-SAR-L2/index.html (accessed on 2017/2/5).
8. Haralick, R. M., K. Shanmugam, and I. Dinstein, "Textural feature for image classification," *IEEE Transactions on Systems, Man and Cybernetics*, SMC-3, No. 6, 610–621, 1973.
9. Dell'Aqua, F. and P. Gamba, "Texture-based characterization of urban environments on satellite SAR images," *IEEE Transactions on Geoscience and Remote Sensing*, Vol. 28, 540–552, 2003.
10. Kandaswamy, U., D. A. Adjeroh, and M. C. Lee, "Efficient texture analysis of SAR imagery," *IEEE Transactions on Geoscience and Remote Sensing*, Vol. 43, No. 9, 2075–2083, 2005.
11. Shimada, M., "Model-based Polarimetric SAR calibration method using forest and surface scattering targets," *IEEE Transaction of Geoscience and Remote Sensing*, Vol. 49, No. 5, 1712–1733, 2011.
12. Lee, J. S., "Digital image enhancement and noise filtering by use of local statistics," *IEEE Transaction on Pattern Analysis and Machine Intelligence*, Vol. 2, No. 2, 165–168, 1980.
13. JAXA ALOS project, "High-resolution land-use and land-cover map of Japan: version 16.09," http://www.eorc.jaxa.jp/ALOS/lulc/jlulc_jpn.htm (accessed on 2017/2/13).
14. Takahashi, M., K. N. Nasahara, T. Tadono, T. Watanabe, M. Dotsu, T. Sugimura, and N. Tomiyama, "JAXA high resolution land-use and land-cover map of Japan," *Proc. of IGARSS 2013, IEEE*, 2384–2387, 2013.